Nanoparticle Optics: The Importance of Radiative Dipole Coupling in Two-Dimensional Nanoparticle Arrays†

Christy L. Haynes, Adam D. McFarland, LinLin Zhao, Richard P. Van Duyne, and George C. Schatz*

Department of Chemistry, Northwestern University, 2145 Sheridan Road, Evanston, Illinois 60208

Linda Gunnarsson, Juris Prikulis, Bengt Kasemo, and Mikael Käll

Department of Applied Physics, Chalmers University of Technology, S-412 96 Göteborg, Sweden

Received: January 29, 2003; In Final Form: February 26, 2003

In this paper, the electromagnetic interactions between noble metal nanoparticles are studied by measuring the extinction spectra of two-dimensional arrays of Au and Ag cylinders and trigonal prisms that have been fabricated with electron beam lithography. The nanoparticles are typically 200 nm in diameter and 35 nm in height; both hexagonal and square array patterns have been considered with lattice spacings that vary from 230 to 500 nm. The extinction spectra typically have a maximum in the 700−800 nm region of the spectrum, and this maximum blue shifts as lattice spacing is reduced, having typically a 40 nm decrease in λ_{max} for a 100 nm decrease in lattice spacing. The results are similar for the different noble metals, array patterns, and nanoparticle shapes. The extinction spectra have been modeled using coupled dipole calculations, and the observed spectral variations are in good qualitative agreement with experimental data. Moreover, the computational analysis indicates that the blue shifts are due to radiative dipolar coupling between the nanoparticles and retardation effects. These effects result in a net depolarization of the dipole couplings for lattice spacings of 200−500 nm.

Introduction

To satisfy the technological demand for ever-decreasing device feature sizes and ever-increasing device performance, it is imperative to explore size-dependent chemical and physical properties. The optical,[1−4] magnetic,[5] catalytic,[6] thermodynamic,[7] electrical transport,[8] and electrochemical[9] properties of nanoscale materials differ significantly from the properties found in their bulk, molecular, or atomic counterparts. Studies of nanoscale noble metal materials are especially important because these materials have potential as optical filters,[10] plasmonic waveguides,[11] bio/chemosensors,[12,13] and substrates for surface-enhanced spectroscopies.[14,15] Because of interest in nanoparticle-based devices, many research groups are currently fabricating and studying nanoparticle arrays. Chumanov and co-workers have studied nanoparticle coupling effects by dispersing nanoparticles onto polymer-coated quartz substrates.[16] The varying lattice spacing between the randomly dispersed nanoparticles prohibits a thorough understanding of the relation between nanoparticle arrangement and the optical properties of the array. The extinction spectra of Ag and Au nanowire gratings of various dimensions and square arrays of Au cylinders have been studied by Aussenegg and co-workers.[17−19] Atwater and co-workers have studied one-dimensional arrays of Au spheroidal nanoparticles for application as optical waveguides.[20,21] Other research groups have focused on the optical properties of two-dimensional arrays to utilize these nanoparticle assemblies as surface-enhanced spectroscopy substrates.[22−25]

The work presented herein utilizes two-dimensional noble metal nanoparticle arrays fabricated using electron beam lithography (EBL) to systematically probe the effect of electromagnetic coupling on the localized surface plasmon resonance (LSPR). The LSPR is a collective oscillation of the nanoparticle conduction electrons.[26] This oscillation can be localized on a single nanoparticle, or it may involve many coupled nanoparticles. The electron oscillation frequency is highly dependent on the effective size and shape of the noble metal nanostructure, and it also depends on nanoparticle arrangement and separation. The LSPR for noble metal nanoparticles in the 20 to a few hundred nanometer size regime occurs in the visible and IR regions of the spectrum and can be measured by UV−visible−IR extinction spectroscopy.[3]

Nanoscale devices are likely to require assemblies of nanoparticles for functionalities that include sensing and waveguide applications. The design of plasmonic nanodevices relies heavily on the nature of the electromagnetic interactions between nanoparticles in the devices. These interactions can be evaluated by measuring the LSPR wavelength because an explicit LSPR peak shift occurs as the electromagnetic coupling changes, that is, when nanoparticles come closer together or further apart. Some aspects of these electromagnetic interactions are well understood. For example, the LSPR wavelength of a pair of nanoparticles exhibits a red shift when the nanoparticles approach and the polarization of the incident light is parallel to the interparticle axis, while blue shifting occurs when the polarization is perpendicular to the axis.[27] This can easily be explained in terms of static dipolar coupling between the nanoparticles. Parallel polarization leads to collinear induced dipoles where fields constructively add to the applied field, thus

† Part of the special issue "Arnim Henglein Festschrift".

* To whom correspondence should be addressed. E-mail: schatz@chem.northwestern.edu.

10.1021/jp034234r CCC: $25.00
Published on Web 05/01/2003

achieving resonance at lower frequencies. Alternately, perpendicular polarization leads to destructive interaction with the applied field, and therefore, higher frequency resonances. The consequences of static dipolar interactions for planar arrays is known from the work by Murray and Bodoff[28] in which red shifts were observed for coupled vibrational dipoles in planar arrays with in-plane polarization. These interactions have also been considered in three dimensions; Lazarides and Schatz[29] demonstrated that red shifts occur for three-dimensional cubic arrays of 13 nm gold nanoparticles with separations of 5−15 nm (separations small enough that electrostatic interactions should dominate). However, for other nanoparticle configurations and for nanoparticle separations comparable with a wavelength of light, electromagnetic coupling between nanoparticles can lead to more complex behavior. Computational modeling is employed to explore this behavior in a companion paper.[30] This complimentary work illustrates the complex behavior of a planar array of spherical nanoparticles as a function of lattice spacing. With in-plane polarization, a decrease in lattice spacing yields a LSPR blue shift for large separations (>100 nm) but a LSPR red shift for smaller lattice spacing. Whereas red shifts are the expected result for static dipolar interactions (which have a $1/d^3$ dependence on nanoparticle separation), the blue shifts demonstrate the importance of radiative dipolar coupling (which has a $1/d$ dependence on nanoparticle separation) and retardation (which multiplies the dipole field by e^{ikd}) for large interparticle separations.

The present paper provides experimental evidence for this long-range coupling mechanism using a variety of two-dimensional nanoparticle arrays fabricated with EBL. EBL readily lends itself to precision control of nanoparticle features and arbitrary array geometry,[31] which is ideal for studying electromagnetic coupling. Because the nanoparticles produced by EBL for this work are cylinders or trigonal prisms, the work in ref 30 has been extended to allow for computational modeling of dipolar coupling of spheroidal nanoparticles. The present work presents the most complete, systematic study of interparticle coupling by pairing experimental measurements with coupled dipole simulations.

Experimental Methods

A. Sample Fabrication. The samples were prepared by EBL on soda glass substrates. First, the clean glass substrate was spin-coated with a 70 nm thin film of an electron-sensitive resist, ZEP 520 (Nippon ZEON Ltd.) diluted 1:2 in methoxybenzene. Before the pattern was exposed, the resist film was coated with a 10 nm thin film of gold to make the surface conductive. During patterning, the electron beam passes straight through this thin metal coating and exposes the resist as desired. The resolution of the EBL system used (JEOL JBX5D-II) is approximately 20 nm, employing an accelerating voltage of 50 kV. After exposure, the Au film was removed by etching in an aqueous solution of 4 g of KI and 1 g of I_2 in 150 mL of deionized water.[32] The patterns were then developed in xylene, creating a patterned resist film on top of which the metal (Ag or Au) was deposited in a high-vacuum thin film vapor deposition system (AVAC HVC 600). The deposited thickness and deposition rate were measured by a quartz crystal microbalance. The deposition rate was maintained at ~1 Å/s to create a smooth film. In the last step of the sample preparation, the lift-off step, the resist was dissolved in a strong solvent (Shipley remover 1165), which also removes the metal deposited on top of the resist. To ensure that the metal film on top of the resist does not have any physical contact with the metal deposited directly on the substrate, samples were prepared with an "undercut" in the resist film. This is accomplished by overdeveloping the resist slightly.

TABLE 1: Characteristics of Nanoparticle Arrays

shape	arrangement	size [nm][a]	material	grating periods [nm]
circular	hexagonal	200	Au	230, 260, 280, 300, 325, 350, 400, 450, 500
circular	hexagonal	200	Ag	260, 280, 300 325, 350, 400, 450, 500
circular	square	200	Au	250, 300, 350, 400, 450, 500
circular	square	200	Ag	300, 350, 450, 500
triangular	hexagonal	170	Au	280, 300, 325, 350, 400, 450, 500
triangular	hexagonal	170	Ag	280, 300, 325, 350, 400, 450, 500

[a] All 35 nm in height.

In this work, 60 μm × 60 μm arrays of Ag or Au nanoparticles were prepared with varied shapes and arrangements. Keeping all of the other parameters in the array constant, we have varied the lattice spacing of the array from near contact to a few hundred nanometer separation. The arrays fabricated for this study are summarized in Table 1.

B. Optical Characterization of Nanoparticle Arrays. The extinction measurements reported here were recorded with an Ocean Optics model S2000 spectrometer over the range 350−850 nm. The spectrometer was fiber-optically coupled to a Nikon TE300 inverted microscope. White light from the TE300 lamp was collimated before being passed through the sample. The transmitted light was collected with a 20× (NA = 0.5) objective. The light was then spatially filtered at the image plane on the side port of the microscope before being focused into the 400 μm core diameter fiber coupled to the spectrometer. Because of the spatial filtering, the probed spot size was approximately 50 μm in diameter at the sample. Data processing included boxcar smoothing and identification of the extinction maximum (λ_{max}) using a derivative routine.

C. Structural Characterization of Nanoparticle Arrays. The EBL patterns were characterized using scanning electron microscopy (JEOL JSM-6301F), and the height of the nanoparticles were determined by atomic force microscope (AFM) measurements. In Figure 1, images of different shapes and arrangements are shown. All of the EBL fabrication and most of the structural characterization were carried out in the MC2 process lab at Chalmers University of Technology.

Results

A. Experimental Results. Figure 2 shows the extinction spectra for hexagonal arrays of Au and Ag cylinders (diameter (D) = 200 nm, height (h) = 35 nm, and lattice spacing (d) = 230−500 nm). This shows the expected LSPR extinction maximum (λ_{max}) in the 700−800 nm range; the measured λ_{max} blue shifts as the nanoparticle separation decreases for both Au and Ag nanoparticle arrays. The wavelength of the λ_{max} shifts 42 and 43 optical nm for a 100 nm change in nanoparticle lattice spacing for the Au and Ag arrays, respectively.

Figure 3 shows the corresponding extinction spectra for square arrays of Au and Ag cylinders (D = 200 nm, h = 35 nm, and d = 250−500 nm). Here, the extinction λ_{max} shifts 62 and 55 optical nm for a 100 nm change in nanoparticle lattice spacing for the Au and Ag arrays, respectively. On the basis of the linear regressions, the coupling effects appear to be slightly more significant in the square arrays.

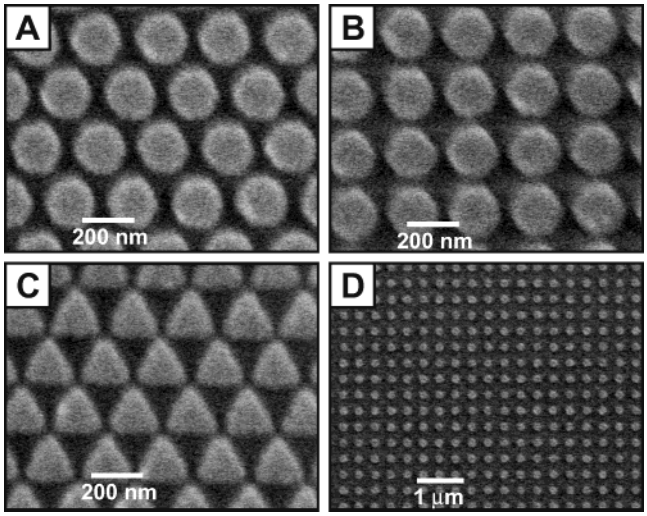

Figure 1. Scanning electron micrographs of representative nanoparticle arrays (all 35 nm in height): (A) cylindrical nanoparticles with a diameter of 200 nm in hexagonal arrangement, period 260 nm; (B) cylindrical nanoparticles with a diameter of 200 nm in square arrangement, period 250 nm; (C) trigonal prism nanoparticles with a perpendicular bisector of 170 nm in hexagonal arrangement, period 230 nm; (D) cylindrical nanoparticles with a diameter of 200 nm in square arrangement, period 350 nm.

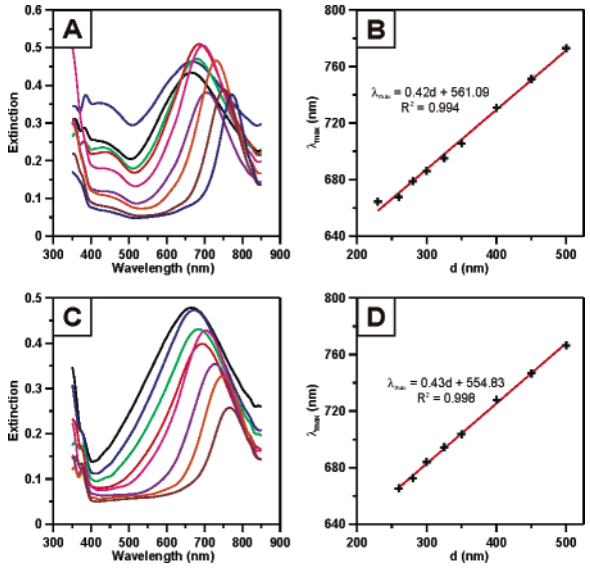

Figure 2. Measured extinction spectra of Au and Ag cylinders in hexagonal arrays (D = 200 nm, h = 35 nm) with varied nanoparticle spacing: (A) Au cylinders, black line = 230 nm, blue line = 260 nm, green line = 280 nm, red line = 300 nm, pink line = 325 nm, purple line = 350 nm, orange line = 400 nm, brown line = 450 nm, and navy line = 500 nm; (B) corresponding plot of lattice spacing (d) versus LSPR λ_{max}; (C) Ag cylinders, black line = 260 nm, blue line = 280 nm, green line = 300 nm, red line = 325 nm, pink line = 350 nm, purple line = 400 nm, orange line = 450 nm, and brown line = 500 nm; (D) corresponding plot of lattice spacing (d) versus LSPR λ_{max}.

Figure 4 shows the extinction spectra for hexagonal arrays of Au and Ag trigonal prisms (a = 170 nm, h = 35 nm, and d = 280−500 nm). The extinction spectra still show a maximum for wavelengths in the 700−800 nm range, and the λ_{max} shifts 36 and 35 optical nm for a 100 nm change in nanoparticle lattice spacing for the Au and Ag arrays, respectively. The λ_{max} of the array of trigonal prisms shows a slightly smaller dependence on lattice spacing than that of the array of cylinders. Note also that there are well-defined LSPR features near 500 nm for Ag and 570 nm for Au. By analogy with what has previously been

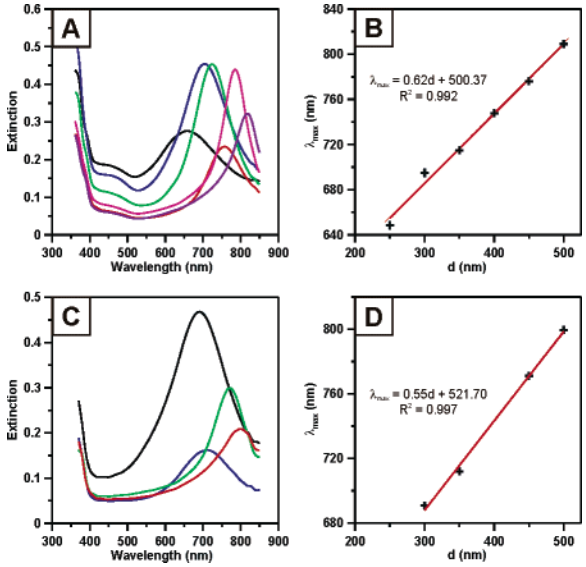

Figure 3. Measured extinction spectra of Au and Ag cylinders in square arrays (D = 200 nm, h = 35 nm) with varied nanoparticle spacing: (A) Au cylinders, black line = 250 nm, blue line = 300 nm, green line = 350 nm, red line = 400 nm, pink line = 450, and purple line = 500 nm; (B) corresponding plot of lattice spacing (d) versus LSPR λ_{max}; (C) Ag cylinders, black line = 300 nm, blue line = 350 nm, green line = 450 nm, and red line = 500 nm; (D) corresponding plot of lattice spacing (d) versus LSPR λ_{max}.

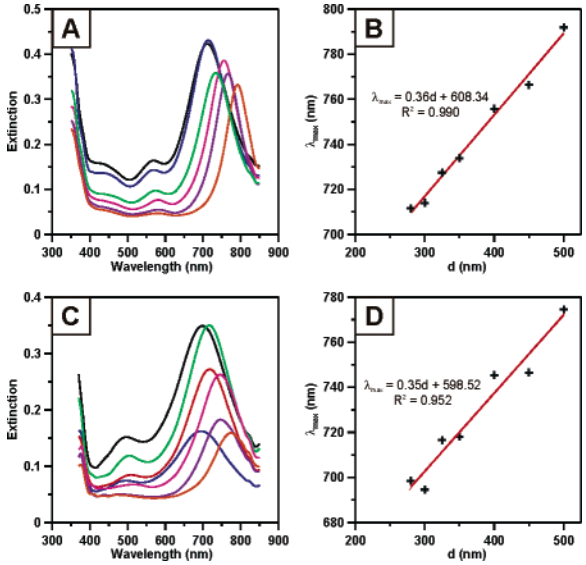

Figure 4. Measured extinction spectra of Au and Ag trigonal prisms in hexagonal arrays (D = 200 nm, h = 35 nm) with varied nanoparticle spacing: (A) Au trigonal prisms, black line = 280 nm, blue line = 300 nm, green line = 325 nm, red line = 350 nm, pink line = 400 nm, purple line = 450 nm, and orange line = 500 nm; (B) corresponding plot of lattic spacing (d) versus LSPR λ_{max}; (C) Ag trigonal prisms, black line = 280 nm, blue line = 300 nm, green line = 325 nm, red line = 350 nm, pink line = 400 nm, purple line = 450 nm, and orange line = 500 nm; (D) corresponding plot of lattice spacing (d) versus LSPR λ_{max}.

observed for trigonal prisms in solution,[33] these features are assigned to in-plane quadrupole resonances. These resonances have a weaker dependence on lattice spacing than the corresponding dipole resonances at 700−800 nm, but blue shifts are also observed as lattice spacing decreases. A detailed analysis of the behavior of the quadrupolar resonance is a subject of future work.

B. Theory: Coupled Dipole Approximation. To model the presented experimental results, coupled dipole approximation

(CDA) calculations have been performed for arrays of oblate Ag spheroids that have dimensions similar to those of the cylinders fabricated by EBL. The CDA is a numerical method for solving Maxwell's equations, which can generate the absorption, scattering, and extinction cross sections for arrays and aggregates of nanoparticles. It assumes that (1) each component nanoparticle only interacts with the electric dipole component of the local field (i.e., higher order multipole resonances are not described), (2) the local field at any nanoparticle is the sum of the incident plane wave field and the scattered field from the other nanoparticles, and (3) the response of the aggregate involves self-consistent determination of the response of each nanoparticle to its local field from the other nanoparticles. Thus, for an array with N nanoparticles, the polarizability of each nanoparticle is based on bulk dielectric constants and the induced polarizations are determined by solving self-consistently for the sum of the incident field and the retarded dipole field of the other $N - 1$ nanoparticles. Full details of this method have been described in the companion paper.[30] It is important to note, however, that here the nanoparticles are modeled as oblate spheroids rather than spheres. The expression for the spheroid polarizability, α (the component associated with polarization along the major axes), was taken from previous work.[34] In this expression, we have corrected the quasistatic polarizability for radiative damping and dynamic depolarization effects, using an expression developed by Zeman and Schatz.[35] The accuracy of this treatment for spheroid electrodynamics was recently studied by making comparisons with exact spheroid results,[34] and it was found to provide an excellent approximation for isolated particles. However, it is possible that radiative damping effects may be smaller for the nanoparticle arrays when, as is the case with our arrays, all diffraction orders are evanescent. This effect was observed in recent studies of plasmon absorption in noble metal wire arrays,[36] and it could lead to underestimation of particle coupling effects in the CDA result.

It should be noted that, in addition to the treatment of damping, there are three important approximations in our CDA description. Using spheroidal nanoparticle shapes provides a convenient approach to generating the needed polarizability information, and it makes it easy to adjust nanoparticle dimensions to analyze the shape and size dependence of the results. However, this means that the topography of the EBL structures will not be modeled very accurately. The companion paper provides a detailed analysis of multipolar effects for spheres and shows that the CDA is adequate for large nanoparticle separations but becomes less accurate as lattice spacing is decreased. Accordingly, the presented theoretical results are most reliable for the larger lattice spacings considered. The final approximation is the omission of the glass substrate in the calculations. Previous theoretical studies of substrate effects on the LSPR λ_{max} demonstrated that the increased refractive index (relative to air) in contact with the nanoparticles causes the LSPR to red shift.[37] While it is possible to incorporate this effect using effective medium approximations, the present application approximates the nanoparticle shape, making the precise details of such red shifts difficult to determine (i.e., one can compensate between the effect of nanoparticle shape and effective medium to give comparable LSPR λ_{max}). On the basis of these approximations, one can only expect the theoretical analysis to provide a qualitative description of the experimental results.

For all of the calculations presented in this paper, each nanoparticle was represented as an oblate ellipsoid with the major and minor axes chosen to be 200 and 40 nm, respectively

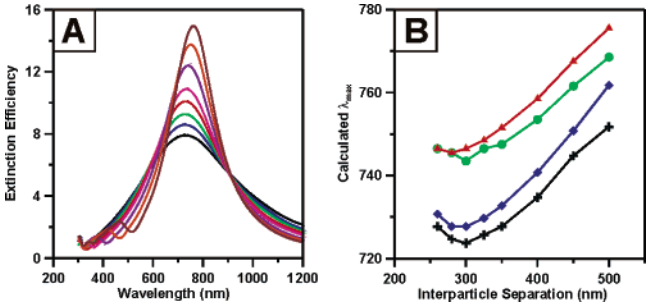

Figure 5. Calculated (A) extinction spectra of Ag nanoparticle arrays in a square lattice using CDA (the interparticle spacing is black line = 260 nm, blue line = 280 nm, green line = 300 nm, red line = 325 nm, pink line = 350 nm, purple line = 400 nm, orange line = 450 nm, and brown line = 500 nm) and (B) λ_{max} as a function of interparticle spacing (black crosses = Ag, hexagonal lattice; blue diamonds = Ag, square lattice; green circles = Au, hexagonal lattice; red triangles = Au, square lattice).

(approximately the same dimensions as the EBL-fabricated Ag cylinders). Nanoparticles with minor axes of 35 nm were also studied, but better quantitative agreement was obtained with 40 nm axes. The great variety of approximations in the model dictates that this parameter choice will not significantly alter the qualitative behavior of the predicted optical properties. The nanoparticles were arranged in either a hexagonal or square pattern to correspond with the EBL-fabricated arrays. The wavelength-dependent dielectric constants for Ag and Au were obtained from Palik.[38]

C. Electrodynamics Results and Comparisons with Experiment. Figure 5A presents extinction spectra calculated using the CDA for the square array of nanoparticles with lattice spacings between 260 and 500 nm. The intensities in this plot refer to the extinction efficiency, which is the ratio of the extinction cross section to the sum of the areas of all of the nanoparticles in the array. Calculations have been done for arrays that have a fixed size corresponding to a circle with a radius of 2 μm. In ref 30, other methods were examined for defining pattern structure, such as fixing the number of nanoparticles while varying the lattice spacing. The resulting spectra were almost identical and thus are not considered here.

Figure 5A shows that the calculated LSPR λ_{max} occurs between 700 and 800 nm for these arrays, which quite closely matches what is observed in the experiment. Such good agreement is probably accidental given the approximations in the CDA model noted above; however, it confirms that the model captures the basic physical effects expected. Note that the spectra show blue shifts as lattice spacing is decreased, as well as some variation in LSPR width and intensity (vida infra).

In Figure 5B, the λ_{max} is plotted versus lattice spacing, d, for hexagonal and square arrays of both Ag and Au nanoparticles. This figure indicates blue shifts for lattice spacings larger than 300 nm but red shifts for smaller lattice spacing. The blue shifts are consistently found for the two different array patterns, the higher density hexagonal lattice giving spectra that are somewhat bluer than the lower density square lattice. Also, the Au λ_{max} results are consistently redder than the Ag λ_{max} results. Except for the slight red shift at small lattice spacing, all of the results in Figure 5B are in good qualitative, but not quantitative, agreement with experimental data. The slope of the curve corresponds to a change in λ_{max} of about 20 nm between 400 and 500 nm lattice spacing, which is about half of that observed in the experimental measurements.

In the companion paper,[30] a semianalytical method was introduced to analyze nanoparticle coupling effects; this analysis

TABLE 2: Lattice Sum, *S*, and Its $1/d^3$ and $1/d$ Contributions for a Square Lattice as a Function of λ/d

λ/d	S	$S(1/d^3)$	$S(1/d)$
1.5	−18.56 − 23.12i	−7.45 + 0.91i	−11.12 − 24.03i
2.0	−16.80 − 1.19i	−3.60 + 4.70i	−13.20 − 5.89i
2.5	−11.17 + 5.25i	−1.04 + 5.25i	−10.13 + 0.00i
3.0	−7.03 + 7.20i	0.52 + 5.05i	−7.56 + 2.15i

describes the variation of the spectra with lattice spacing and pattern in terms of a dimensionless lattice sum, *S*. This lattice sum is given by

$$S = d^3 \sum_{j \neq i} \left[\frac{(1 - ikd_{ij})(3\cos^2\theta_{ij} - 1)\, e^{ikd_{ij}}}{{d_{ij}}^3} + \frac{k^2 \sin^2\theta_{ij}\, e^{ikd_{ij}}}{d_{ij}} \right] \quad (1)$$

where d_{ij} is the distance between nanoparticles labeled *i* and *j* (*d* is the lattice spacing), θ_{ij} is the angle between the polarization vector (assumed to be in the plane of the array) and the vector from nanoparticle *i* to *j*, and $k = 2\pi/\lambda$. The lattice sum is over all of the nanoparticles in the lattice, and the theory applies to an infinite lattice so that any nanoparticle can be chosen to be the *i*th nanoparticle. It was demonstrated that the real part of *S* determines the shift in λ_{max}, positive values corresponding to red shifts and negative values to blue shifts. In addition, the imaginary part of *S* determines the LSPR line width, positive values giving broadened line shapes (compared to the single nanoparticle line shape) and negative values giving narrowed line shapes. This behavior assumes that the dielectric constant of the metal nanoparticle has a real component that is large in absolute value compared to its imaginary part; this condition is adequately satisfied for the LSPRs of interest in the present study. Note also that *S* is weighted by $1/d^3$ in its contributions to the spectra, such that in the large *d* limit the isolated particle result is recovered.

The expression for *S* contains two terms, the first one having a $1/d^3$ dependence on lattice spacing and the second a $1/d$ dependence. Each of these terms has additional dependence on *d*, and in particular, the $e^{ikd_{ij}}$ factor in each term (which measures the importance of retardation) leads to complex contributions to *S* from each term. However, as a simplification, one can regard the $1/d^3$ terms as contributing to short-range interactions between the nanoparticles and the $1/d$ term (the *radiative dipolar interaction*) to long-range interactions.

Values of *S*, as well as its $1/d^3$ and $1/d$ components are tabulated in Table 2 for a range of λ/d that is relevant to the present problem. Because λ is approximately 750 nm and *d* varies from 250 to 500 nm, the range of λ/d is chosen to be 1.5 to 3. The analysis shows that the real part of *S* is consistently negative, which is consistent with the observed blue shift. The real part becomes less negative as λ/d increases, and indeed, it becomes positive for still larger λ/d, indicating that a transition from blue shifting to red shifting should occur for smaller lattice spacing. This transition is evident in Figure 5B, but the experimental results do not exhibit the same trend, presumably because of breakdown of the CDA approach. Because it is not possible to make *d* smaller than the nanoparticle diameter, 200 nm, the small *d* limit of the coupled dipole prediction is unachievable for the chosen nanoparticle size. Table 2 also shows that the real part of *S* is predominantly determined by the $1/d$ component of the field, that is, the radiative dipole interaction. This is especially true for the largest values of λ/d, for which the $1/d^3$ only appears in the imaginary part of *S*.

Table 2 also indicates that the imaginary part of *S* is negative for small λ/d and then becomes positive for large λ/d. This explains the trends seen in Figure 5A, in which the LSPR line width is narrowest for the largest lattice spacing. Thus, this would predict that the reddest LSPR in the experiments should be the narrowest, which is the experimental observation. A somewhat less refined comparison with experiment can be made for the LSPR peak intensities. The general trend in the experimental results is that the peak extinction increases with decreasing lattice spacing. The amount of the increase varies a lot, but a typical change is a factor of 2 as lattice spacing decreases from 500 to 250 nm. Figure 5A shows that the peak extinction efficiency decreases with decreased lattice spacing by a factor of 2 over this same range of lattice spacings. To compare theory and experiment, it is necessary to multiply the extinction efficiency by the area of nanoparticles being observed. If the illumination spot size is fixed, then the area of nanoparticles is proportional to the number of nanoparticles in the spot, and this in turn varies as the inverse square of the lattice spacing. Thus, in going from 500 to 250 nm lattice spacing, the number of nanoparticles is quadrupled, and thus, the peak extinction (multiplying the extinction efficiency by the number of nanoparticles) is doubled. This is in agreement with the experimental number noted above.

It is interesting to note that even with the largest lattice spacings studied, both theoretically and experimentally, the expected isolated nanoparticle spectrum was not observed. In the case of the theoretical studies, the influence of radiative coupling effects persists out to lattice spacings at which the lattice sums (for an infinite lattice) are numerically difficult to compute. Future experimental studies will focus on this topic.

Conclusions

This work has demonstrated that the LSPR of Au and Ag nanoparticle arrays exhibit pronounced blue shifts as lattice spacing is decreased. The blue shifts were found to occur for both hexagonal and square lattices with slight differences between lattices. These differences correlate with lattice density such that denser lattices give bluer λ_{max}. In addition, the Au and Ag results are very similar, which demonstrates that these two metals have similar dielectric properties for LSPR in the far-red and near-infrared although they have significant differences in behavior below 700 nm.

The blue shifts are observed for nanoparticle arrays with relatively large lattice spacings (approximately half the LSPR wavelength) for which radiative dipole interactions between the nanoparticles play an important role and retardation effects are large. For smaller lattice spacings (<100 nm), one expects red shifts (for the case in which the electric polarization is in the plane of the array), and indeed such red shifts have been observed for three-dimensional aggregates of Au nanoparticles.[39] For the highly oblate nanoparticles considered in this study, the size of the blue shift is very large, corresponding to a 40 nm shift in λ_{max} for each 100 nm change in the lattice spacing. These shifts are much larger than those calculated for the spheres modeled in ref 30 because the nanoparticles are larger and therefore the polarizabilities are larger. The large wavelength shifts will be useful for biological sensing applications in which analyte binding triggers a change in the array structure. Concomitantly, it should be noted that the nanoparticles used in this work are too large to allow study of small lattice spacings at which red shifts are expected. Thus, in some sensing applications in which the transition from blue shifts to red shifts might be of interest, it will be necessary to use smaller nanoparticles.

Another important result of this paper is the success of computational modeling in interpreting the observed blue shifts

and in rationalizing changes in the line width and intensity of the LSPR as the lattice spacing is varied. This theory provides a simple tool for predicting whether red shifts or blue shifts and narrowing or broadening will occur on the basis of a simple lattice sum that is easily calculated for any configuration of nanoparticles, and thus, it will be generally useful in future studies. The present theory is based on some serious approximations such as point dipoles, the neglect of substrate effects, and the use of spheroidal nanoparticles, so the comparisons of theory and experiment are only qualitative. Therefore, an important challenge for the future will be to develop theories that relax these approximations.

Acknowledgment. We acknowledge support of the Nanoscale Science and Engineering Initiative of the National Science Foundation under NSF Award Number EEC-0118025. Any opinions, findings, and conclusions or recommendations expressed in this material are those of the author(s) and do not necessarily reflect those of the National Science Foundation. We also acknowledge the support of the Air Force Office of Scientific Research Multidisciplinary University Research Initiative program (Grant F49620-02-1-0381). C.L.H. acknowledges the support of a Northwestern University Presidential Fellowship. L.G., J.P., B.K., and M.K. acknowledge financial support from the Swedish Research Council and the Swedish Foundation for Strategic Research.

References and Notes

(1) Mulvaney, P. *Langmuir* **1996**, *12*, 788−800.
(2) Feldstein, M. J.; Keating, C. D.; Liau, Y. H.; Natan, M. J.; Scherer, N. F. *J. Am. Chem. Soc.* **1997**, *119*, 6638−6647.
(3) Haynes, C. L.; Van Duyne, R. P. *J. Phys. Chem. B* **2001**, *105*, 5599−5611.
(4) Link, S.; Mohamed, M. B.; El-Sayed, M. A. *J. Phys. Chem. B* **1999**, *103*, 3073−3077.
(5) Shi, J.; Gider, S.; Babcock, K.; Awschalom, D. D. *Science* **1996**, *271*, 937−941.
(6) Street, S. C.; Xu, C.; Goodman, D. W. *Annu. Rev. Phys. Chem.* **1997**, *48*, 43−68.
(7) Wang, Z. L.; Petroski, J. M.; Green, T. C.; El-Sayed, M. A. *J. Phys. Chem. B* **1998**, *102*, 6145−6151.
(8) Andres, R. P.; Bielefeld, J. D.; Henderson, J. I.; Janes, D. B.; Kolagunta, V. R.; Kubiak, C. P.; Mahoney, W. J.; Osifchin, R. G. *Science* **1996**, *273*, 1690−1693.
(9) Gorer, S.; Ganske, J. A.; Hemminger, J. C.; Penner, R. M. *J. Am. Chem. Soc.* **1998**, *120*, 9584−9593.
(10) Dirix, Y.; Bastiaansen, C.; Caseri, W.; Smith, P. *Adv. Mater.* **1999**, *11*, 223−227.
(11) Knoll, W. *Annu. Rev. Phys. Chem.* **1998**, *49*, 569−638.
(12) Storhoff, J. J.; Elghanian, R.; Mucic, R. C.; Mirkin, C. A.; Letsinger, R. L. *J. Am. Chem. Soc.* **1998**, *120*, 1959−1964.
(13) Haes, A. J.; Van Duyne, R. P. *J. Am. Chem. Soc.* **2002**, *124*, 10596−10604.
(14) Kahl, M.; Voges, E.; Kostrewa, S.; Viets, C.; Hill, W. *Sens. Actuators, B* **1998**, *51*, 285−291.
(15) Freeman, R. G.; Grabar, K. C.; Allison, K. J.; Bright, R. M.; Davis, J. A.; Guthrie, A. P.; Hommer, M. B.; Jackson, M. A.; Smith, P. C.; Walter, D. G.; Natan, M. J. *Science* **1995**, *267*, 1629−1632.
(16) Malynych, S.; Luzinov, I.; Chumanov, G. *J. Phys. Chem. B* **2002**, *106*, 1280−1285.
(17) Felidj, N.; Aubard, J.; Levi, G.; Krenn, J. R.; Schider, G.; Leitner, A.; Aussenegg, F. R. *Phys. Rev. B: Condens. Matter Mater. Phys.* **2002**, *66*, 245407/245401−245407/245407.
(18) Schider, G.; Krenn, J.; Gotschy, W.; Lamprecht, B.; Ditlbacher, H.; Leitner, A.; Aussenegg, F. *J. Appl. Phys.* **2001**, *90*, 3825−3830.
(19) Lamprecht, B.; Schider, G.; Lechner, R. T.; Ditlbacher, H.; Krenn, J. R.; Leitner, A.; Aussenegg, F. R. *Phys. Rev. Lett.* **2000**, *84*, 4721−4724.
(20) Maier, S. A.; Brongersma, M. L.; Kik, P. G.; Atwater, H. A. *Phys. Rev. B* **2002**, *65*, 193408/193401−193408/193404.
(21) Maier, S. A.; Kik, P. G.; Atwater, H. A. *Appl. Phys. Lett.* **2002**, *81*, 1714−1716.
(22) Gunnarsson, L.; Bjerneld, E. J.; Xu, H.; Petronis, S.; Kasemo, B.; Kall, M. *Appl. Phys. Lett.* **2001**, *78*, 802−804.
(23) Jensen, T. R.; Schatz, G. C.; Van Duyne, R. P. *J. Phys. Chem. B* **1999**, *103*, 2394−2401.
(24) Felidj, N.; Aubard, J.; Levi, G.; Krenn, J. R.; Salerno, M.; Schider, G.; Lamprecht, B.; Leitner, A.; Aussenegg, F. R. *Phys. Rev. B* **2002**, *65*, 075419/075411−075419/075419.
(25) Haynes, C. L.; Van Duyne, R. P. *J. Phys. Chem. B*, in press.
(26) Schatz, G. C.; Van Duyne, R. P. In *Handbook of Vibrational Spectroscopy*; Chalmers, J. M., Griffiths, P. R., Eds.; Wiley: New York, 2002; Vol. 1, pp 759−774.
(27) Jensen, T.; Kelly, L.; Lazarides, A.; Schatz, G. C. *J. Cluster Sci.* **1999**, *10*, 295−317.
(28) Murray, C. A.; Bodoff, S. *Phys. Rev. Lett.* **1984**, *52*, 2273−2276.
(29) Lazarides, A. A.; Schatz, G. C. *J. Phys. Chem. B* **2000**, *104*, 460−467.
(30) Zhao, L.; Kelly, K. L.; Schatz, G. C. *J. Phys. Chem. B* **2003**, *107*, 7343−7350.
(31) Ito, T.; Okazaki, S. *Nature* **2000**, *406*, 1027−1031.
(32) Eidelloth, W.; Sandstrom, R. L. *Appl. Phys. Lett.* **1991**, *59*, 1632−1634.
(33) Jin, R.; Cao, Y.; Mirkin, C. A.; Kelly, K. L.; Schatz, G. C.; Zheng, J. G. *Science* **2001**, *294*, 1901−1903.
(34) Kelly, K. L.; Coronado, E.; Zhao, L. L.; Schatz, G. C. *J. Phys. Chem. B* **2003**, *107*, 668−677.
(35) Zeman, E. J.; Schatz, G. C. *J. Phys. Chem.* **1987**, *91*, 634−643.
(36) Schider, G.; Krenn, J. R.; Gotschy, W.; Lamprecht, B.; Ditlbacher, H.; Leitner, A.; Aussenegg, F. R. *J. Appl. Phys.* **2001**, *90*, 3825−3830.
(37) Duval Malinsky, M.; Kelly, K. L.; Schatz, G. C.; Van Duyne, R. P. *J. Phys. Chem. B* **2001**, *105*, 2343−2350.
(38) Lynch, D. W.; Hunter, W. R. In *Handbook of optical constants of solids*; Palik, E. D., Ed.; Academic Press: New York, 1985.
(39) Storhoff, J. J.; Lazarides, A. A.; Mucic, R. C.; Mirkin, C. A.; Letsinger, R. L.; Schatz, G. C. *J. Am. Chem. Soc.* **2000**, *122*, 4640−4650.